River Water Level Prediction Using Passive Microwave Signatures—A Case Study: The Bermejo Basin

Cristina Vittucci, Leila Guerriero, *Member, IEEE,* Paolo Ferrazzoli, *Senior Member, IEEE,*
Rachid Rahmoune, Verónica Barraza, and Francisco Grings

Abstract—The aim of this work is to investigate the exploitation of radiometric acquisitions from satellite sensors at different microwave frequencies in view of the prediction of river water level. A case study has been identified in the Bermejo basin, in northern Argentina. This river is seasonally affected by severe flooding events in the lower part, mostly due to rains occurring in the upper basin, that produce sediment loadings flushing down along the lower basin thus changing the watercourse. While the effectiveness of microwave radiometry at Ka band for flood monitoring is consolidated in the literature, this study also considers X and C bands (provided by the Advanced Microwave Scanning Radiometer (AMSR) series together with the higher frequency) and highlights the better sensitivity to soil conditions of L band data (made recently available, thanks to SMOS) over moderately and densely vegetated areas. This study confirms, first, the well-known capability of passive microwave remote sensing instruments to record brightness temperature variations due to rainfall and floods occurred near river edges under different seasonal conditions. For this purpose, a multifrequency comparative analysis is conducted. Second, it investigates whether these properties can be exploited for flood forecasting: a model which directly links the daily satellite measurements to the river water level has been tested, considering 1- to 7-day forecast horizons. The results show that forecasting models can take advantage of the sensitivity of low frequencies to soil moisture conditions in order to predict flood peaks, despite the instrument's low resolutions.

Index Terms—Flood, forecasting, hydrology, microwave radiometry.

I. INTRODUCTION

IN the last few decades, several approaches have been applied to predict the river conditions, such as physically based hydrological models [1]–[3] and statistical or data-driven models [4]–[6]. The study of water level stage for flood emergency requires knowledge of the probability of occurrence, the measurements of the water level in upstream gauging stations, and a robust algorithm that is able to show, with the slightest possible uncertainty, the estimation of the water level downstream [7]. Routing models have also been used to compute

downstream discharge, and/or level forecasts that generally tend to be more accurate than rainfall-runoff models [7]. However, routing models partially neglect aspects such as backwater effects, so that spatially distributed rainfall-runoff models have been developed as an extension of hydrological flood routing with the aim of providing estimates of water levels at any point along the river system.

The operational applicability of the above-mentioned methods is constrained by their complexity and, to a large extent, by the requirements of extensive rainfall data, detailed information of basin topography, vegetation, and soil characteristics for the description of the hydrological processes. The most promising approach to obtain these data relies on the exploitation of satellite observations. Several works have recently been focused on assimilation of remote sensing data [8]–[12], which can fulfill the above needs in both spatial and temporal terms.

Active microwave remote sensing can provide high resolution data, so that Synthetic Aperture Radar images have been mainly used as a tool for flood and risk mapping [13]–[16], whereas dealing with the evolution of floods requires a suitable revisit time, as achieved recently by COSMO SkyMed [17], [18]. Interferometry has been proposed to measure surface velocity across a river channel [19], whereas satellite altimetry has been considered a source for surface water elevation information [20].

Passive microwave remote sensing, besides being independent of weather and day light, offers a high temporal resolution, which is one of the main requirements for an appropriate monitoring. In particular, passive data at 36 GHz have been successfully used so far to delineate flood extent [21], [22] on the basis of the so-called M/C Ratio, i.e., the ratio between brightness temperature of a wet (Measurement) pixel and the one of a dry (Calibration) pixel, which is directly related to the fraction of water covered area. The same index has been used as a proxy to estimate river discharge [23], [24] and its application for flood forecasting has also been recently presented [25]. These works take advantage of the large contrast between flooded and non-flooded pixels which can be detected, thanks to the spatial resolution of the order of 10 km [of the high-frequency channels of Advanced Microwave Scanning Radiometer for Earth observing system (AMSR-E)], which is suitable for this application.

In this paper, we intend to explore the applicability of lower frequency radiometry to flood monitoring and forecast. For such data, the water extent is no longer the primary driver of the microwave response, because of the reduced spatial resolution (see Sections III-A and B). Soil moisture changes are sensed instead. This parameter plays a critical role in the processes

related to floods and can be monitored through vegetation canopy, especially at L-band, which is the frequency of the recently launched SMOS satellite and of the forthcoming SMAP mission. After checking the sensitivity of the available passive data over an extended frequency range, a test of flood forecast has been carried out following the approach described by Bindlish *et al.* [26]. Such approach has been selected since remote sensing data can be directly assimilated without retrieval of geophysical parameters. Indeed, it is assumed that this information is contained in the radiometric data themselves.

The study area is in the lower Bermejo basin (Argentina), a hardly accessible region where the scarcity of ground measurements makes the application of routing models problematic because of the complexity of the drainage basin and the high water flow from tributaries. Furthermore, this area has been chosen because floods occur periodically, so that the forecasting exercise has been carried out over two events.

This paper is organized as follows: a description of the site, of the sensors used and the collected data is provided in Sections II and III. A comparative analysis with the aim of assessing the reliability of the multifrequency and multitemporal radiometric data is carried out in Section IV. The results of the forecasting exercise carried out using the radiometric data and the model introduced in [26] are described in Section V. The conclusion and possible further developments are presented in Section VI.

II. SITE DESCRIPTION

The region addressed is the Bermejo River basin in Argentina ($22–27°$S and $58–66°$W) and it is depicted in Fig. 1. The Bermejo River has its head in the Andes Mountains of northwestern Argentina and southern Bolivia, in the department of Tarija. The basin extends over some $123\,000$ km^2 in South-East direction and reaches an overall length of 1450 km. The different weather and topographic conditions in this large basin promote an array of rain forest, humid valleys, and mountain desert in the upper basin, and dry, humid, and gallery forest in the lower basin. The study area, situated in the lower Bermejo basin between north Argentina and the river Paraguay, is approximately included inside a rectangular box of coordinates ($25–27°$S lat, $58–60°$W lon) around the hydro-meteorological station of El Colorado, as shown in Fig. 1. In the lower basin ($72\,971$ km^2), the river is divided in two branches. The smaller one is called Bermejito, a meandering bed often dry that reaches the Chaco province. The larger one, called Teuco or Bermejo Nuevo, marks the provincial boundary between Formosa and Chaco while flowing into the Paraguay River. The water course changes continuously, since this area is subject to several processes of erosion and silting, and receives the medium and coarse material mobilized in the upper basin characterized by a high drainage density. The hydrological regime of the Bermejo River has a marked seasonal variety, characterized by a period of significant flow in the wet season, presenting values close to 75% of runoff in summer, and a minimum flow, decreasing to 11%, in the dry season. The mean discharge recorded at the gauging station of El Colorado is about 408 m^3/s. In the last section of the river, between El Sauzalito and El Colorado stations, the bed slope is very low ($<0.03\%$) with a travel time of about 1 week [27].
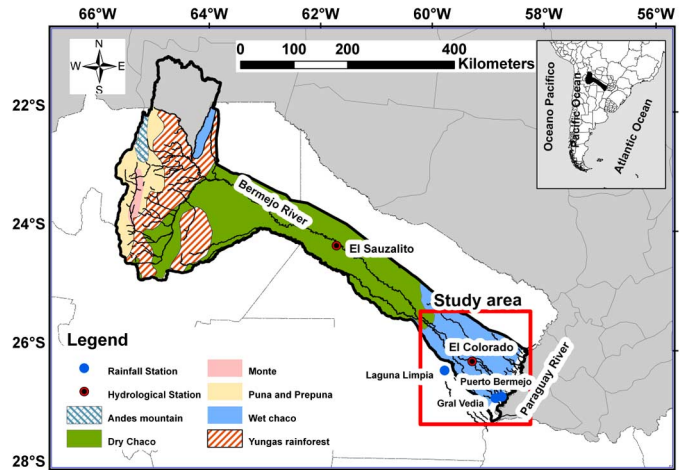

Fig. 1. Bermejo basin location. The rainfall and hydrometric stations considered in this study are marked by circles. The red frame shows the study area of Figs. 3–5.

Annual rainfall in the lower basin is characterized by a decrease from east (1400 mm) to west (300 mm), with highest values in the Paraguay River. The rainy season runs between November and March and it concentrates 85% of total annual precipitation. Average temperatures for this time of year range between $16°C$ and $28°C$, with extreme maximum between $35°C$ and $45°C$, depending on the area. The dry season coincides with Austral Autumn–Winter in the months of June, July, and August when very little or almost no precipitation occurs. Average temperatures in this period range between $8°C$ and $15°C$, with extreme minimum below $0°C$.

In response to precipitation distribution, the Chaco phytogeographic province in Bermejo River basin is divided into two main districts characterized by distinctive tree morphology: 1) the eastern or humid Chaco dominated by Quebracho (*Schinopsis balansae*) and 2) the western or semi-arid Chaco with Red Quebracho (*Schinopsis lorentzii*). The study area lays in the humid Chaco (see Fig. 1). Its wet and humid climate is deposited by northern trade winds, and it is characterized by a strong altitudinal gradient, which corresponds to an important gradient in vegetation species. The plant communities [28] are conditioned by the topographic gradient, and this is related with the flooding pulse. The surroundings of El Colorado station are characterized by crop and herbaceous coverage. The soil conditions are affected, among others, by rainfalls, which were measured in the four meteorological stations (Gral Vedia, Puerto Bermejo, Laguna Limpia, and El Colorado) included in the selected area, whose locations are also shown in Fig. 1.

Indeed, in extended and ramified watersheds lacking diffuse *in situ* network of soil moisture monitoring, as in subtropical South America, the combined use of satellite data and traditional ground based rainfall and water level observations represents a promising alternative to conventional monitoring techniques in the surveillance of flooding phenomena.

III. INSTRUMENTS AND THE DATASETS

Seasonal flooding events often occur during the rainy season in the lower basin of the Bermejo River between the Argentinean

provinces of Chaco and Formosa, due to heavy rains. Depending on the year, floods can occur on a short time interval of 3–4 days, or can last several days. In this respect, the high temporal resolution represents the major attraction of passive microwave data in the detection of floods and in monitoring of the evolution of both short and long events, since they are acquired at a near-global daily coverage. On the other hand, the lower spatial resolution can be considered as the principal weakness, though less stringent for the site under study since the considered phenomena extend over large areas.

Data collected by two passive sensors have been used for this analysis, exploring the phenomena with different wavelengths: AQUA AMSR-E C, X, and Ka bands and SMOS Microwave Imaging Radiometer with Aperture Synthesis (MIRAS) L band. Ground data collected by rain gauges and hydrometric stations were also included in the study. Satellite and ground datasets cover the 2010 and 2011 time frame during which both AMSR-E and SMOS were active: the latter became fully operational in 2010, whereas the first one concluded its lifetime in October 2011. Sensors of the AMSR series are still operating onboard JAXA's Global Change Observation Mission (GCOM) satellite, so that continuity of brightness temperatures acquisitions is guaranteed.

A. AMSR-E Processing

The AMSR-E, aboard NASA's AQUA satellite, provides frequent global coverage of the Earth's surface measuring brightness temperature T_B at six frequencies. Among them, 6.9, 10.7, and 36.5 GHz are the ones considered in this study. The mean spatial resolution on the ground is 56 km at C-band, 38 km at X-band, and 12 km at Ka-band with an incidence angle of 54.8° on the Earth's surface. AMSR-E operates in a Sun-synchronous orbit at 98.2° inclination with ascending equator crossings at 13:30 LT. The imaged swath width is 1445 km, providing full global coverage within 3 days. More detailed information on AMSR-E sensor and its successor AMSR2 onboard JAXA's GCOM—Water (GCOM-W1) satellite can be found in [29] and [30]. Data from AMSR-E level 2 (L2A, version 2, validation level 10) have been gathered for both ascending and descending orbits, at both polarizations, yielding measurements from January 1, 2010 to October 4, 2011, when AMSR-E activity was interrupted. In this paper, only the nighttime AMSR-E observations are used, since soil moisture retrievals based on these data are more reliable than those based on daytime observations [31].

The T_B's at C, X, and Ka bands have been transformed into the corresponding surface emissivities applying the following formula, in the assumption of homogeneous pixel:

$$e_{pf} = \frac{T_{Bpf}}{T_s}. \tag{1}$$

In (1), e and T_B are, respectively, the emissivity and the brightness temperature at the selected frequency f and polarization p (v or h), and T_S is the estimate of the surface temperature. It was demonstrated that the Ka band is the most correlated to surface temperature [32], so that in this work, we used the
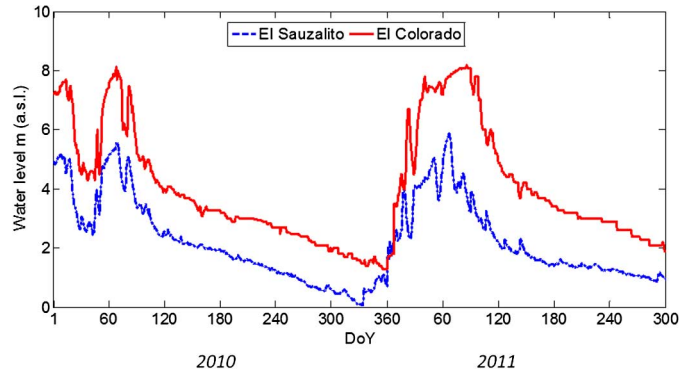

Fig. 2. Bermejo river water level as it was measured at El Colorado and El Sauzalito hydrometric stations during 2010 and 2011.

regression by Parinussa *et al.* [33] developed for the AMSR-E in descending orbit

$$T_s = 0.94 T_{BvK_a} + 30.8 \tag{2}$$

where T_{BvKa} is the measured brightness temperature at Ka band at vertical polarization, and all terms are given in °K. This method provides estimates of the surface temperature with the closest time correspondence to the satellite acquisitions.

B. SMOS Processing

The Soil Moisture and Ocean Salinity (SMOS) ESA satellite provides continuous multiangular measurements of brightness temperature at a frequency of 1.4 GHz [34], [35]. In order to achieve the spatial resolution required for observing soil moisture, a huge antenna would have been required. To overcome this challenge, the MIRAS instrument was developed. The payload is a 2-D interferometer yielding a range of incidence angles from 0° to 55° at both V and H polarizations, and an average resolution of 46 km. SMOS is deployed in a sun-synchronous orbit at 98.44° inclination with ascending equator crossings at 6:00 LT.

Daily L1C observations from ascending and descending orbits have been analyzed for the period 2010–2011. SMOS V.504 data have been used to extract L1C brightness temperatures averaged over observational angles within 37.5° and 47.5°. Data with a distance from swath center higher than 300 km, which showed a poor quality, have been eliminated. Moreover, only data not affected by RFI have been considered. In order to calculate the emissivity applying (1), the surface temperature T_S has been extracted from ECMWF auxiliary products (V.501 version).

C. Hydrometric Data

The area of lower Bermejo basin was subject to severe rain-storms during the analyzed period of time which spans almost 2 years of common operational activity of SMOS and AMSR-E. Fig. 2 reports the water level versus the Day of Year (DoY), as it was measured at two hydrometric stations during the 2010–2011 years. In these sites, seasonal effects, which give rise to two floods, are well visible. Water level at the upstream station of El Sauzalito anticipates peaks and troughs recorded at El Colorado by about 7 days. The peaks in the first parts of the years are due to the rainfalls simultaneously occurring in the whole river basin and, when 6 m water level is reached, they indicate a flooding
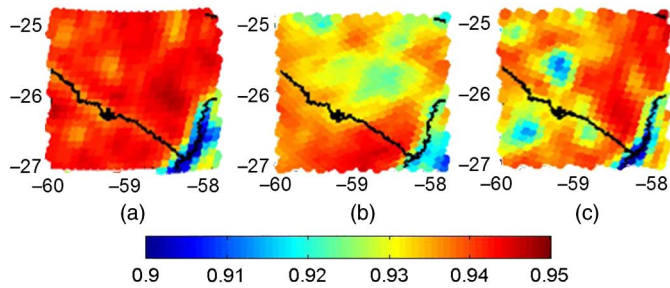
Fig. 3. AMSR-E Ka band maps of horizontal emissivity e_h over lower Bermejo basin in: (a) normal condition; (b) rain condition; and (c) flooding condition.

Fig. 5. AMSR-E C band maps of horizontal emissivity e_h over lower Bermejo basin in: (a) normal condition; (b) rain condition; and (c) flooding condition.
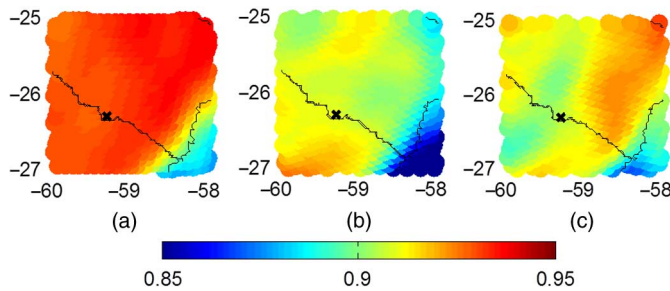

Fig. 4. AMSR-E X band maps of horizontal emissivity e_h over lower Bermejo basin in: (a) normal condition; (b) rain condition; and (c) flooding condition.

Fig. 6. SMOS L-band maps of horizontal emissivity e_h over lower Bermejo basin in: (a) normal condition; (b) rain condition; and (c) flooding condition. (Note the different color scale with respect to Figs. 3 and 4.)

event for the area of El Colorado. At El Sauzalito, the bankfull depth is about 4 m.

During the first months of each year, due to the arrival of the "rainy season" that starts in December and lasts until March, the water level is always high (Fig. 2): at El Colorado station, it is approximately included in a range from 5.5 to 8 m above the sea level (not considering the temporary drop at 4 m after some days of flooding in January 2010), whereas after March, the water level returns under 4 m.

IV. PRELIMINARY ANALYSIS: RAINFALL AND FLOOD EFFECTS OVER THE STUDY AREA

In this section, the sensitivity of brightness temperatures and emissivity to rainfalls and floods is examined at regional and local scale with the aim of highlighting the differences at the various frequency bands.

A preliminary analysis has been performed, producing emissivity maps of the area, extending from 27° to 25° latitude South and 60° to 58° longitude West, around El Colorado hydrometeorological station.

Examples of rain and flooding conditions are provided, and they are compared with the emissivity map produced in absence of storms or discharges and after a rain-free period, from now on called "normal conditions." In the following figures, the Bermejo and Paraguay rivers are drawn in black, whereas the position of El Colorado station is highlighted by a black marker. These maps display night time acquisitions of AMSR-E (descending orbits) and dawn acquisitions of SMOS (ascending orbits), so that the influence of diurnal insolation can be neglected.

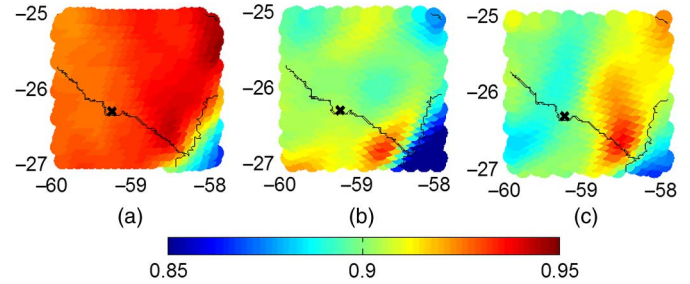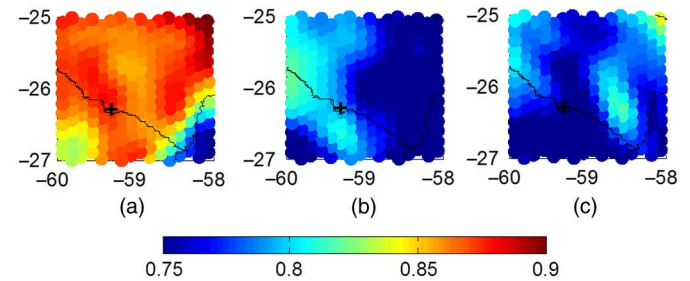In Figs. 3–6, the maps of horizontal polarized emissivity e_h at 36.5, 10.7, 6.9 and 1.4 GHz, respectively, are shown, and the three columns report three different days corresponding to normal, rain, and flooding condition, respectively. For each frequency, the maps show data collected on April 12, 2010 (in the absence of precipitation, after about 10 days from a rain event, and water level of 4.5 m, i.e., under the bankfull height), May 18, 2010 (about 20 mm precipitation at Puerto Bermejo and Gral Vedia, with water level of 2.4 m) and February 26, 2010 (in correspondence of flood). The bottom right corner corresponds to the confluence of the Bermejo River into Rio Paraguay. The latter is imaged in blue shades, from dark to light, depending on the moisture conditions of the areas falling within the AMSR-E and SMOS-MIRAS footprints.

Looking at the maps for the same date, it is possible to observe the overall decreasing trend of emissivity with respect to frequency. Note that, in order to avoid color saturation, and to highlight the sensitivity of the various frequencies, we used different color scales. At the higher frequencies and in normal conditions [Figs. 3(a), 4(a), and 5(a)], the emissivity over El Colorado area reaches quite uniform high values, whereas the higher capability of penetration through vegetation at L-band [Fig. 6(a)] allows to record less-saturated values with higher spatial variability than at shorter wavelengths. Emissivity reductions can be observed at all frequencies in the whole area, in correspondence of the rainfall event [Figs. 3(b), 4(b), 5(b), 6(b)]. In the case of flooding [Figs. 3(c), 4(c), 5(c), 6(c)], the maps show more marked reductions of emissivity with respect to the "rain" images around El Colorado hydrological station, where a water gauge above bankfull is documented. This behavior due to the soil saturation condition is much more evident at L band. The inhomogeneities of e_h, which can be observed at Ka band, are due to spatial inhomogeneities which are visible, thanks to the higher resolution. At C and X bands, the phenomenon affects

mainly the area surrounding El Colorado station, where the flooding produces the major effects. In the same maps, the eastern areas, closer to Rio Paraguay, show intermediate emissivity values between rain and normal conditions.

The same trends have been confirmed by the vertical polarization emissivity maps, but with higher average values (not shown here).

An assessment of the previous results has been carried out considering the T_B trends at all considered bands, averaging measurements over a portion of half degree × half degree, between 26° and 26.5°S latitude and 59° and 59.5°W longitude, i.e., about 50×50 km just around El Colorado station. The selection of this area allowed studying the effects of soil moisture variation during flooding events, which may extend far away the watershed. Although soil moisture measurements were not available for the site under study, in [36], a clear correlation between the rain occurrence and the soil moisture content provided by ECMWF over the same area has been observed. For this reason, in Fig. 7, the daily rainfall data coming from the four meteorological stations in the Bermejo area are plotted together with the average T_{Bv} and T_{Bh} measured by both radiometers.

Fig. 7(a)–(c) shows the comparison between the intensities of measured rainfalls and the AMSR-E 2010–2011 series of brightness temperature for descending orbits at both polarizations at Ka, X, and C bands, respectively. As previously mentioned, response to rain events is more apparent during nighttime passes, because less affected by insolation issues [23]. In Fig. 7(d), the same comparison is shown considering the L band dual polarization brightness temperature series acquired by SMOS in both ascending and descending orbits (because of the reduced amount of noise-free data). The long term trend of T_B is dependent on the season: an absolute minimum can be identified during the dry season, i.e., from June to August ($\text{DoY} = 150 - 250$), whereas the maximum values can be observed at the beginning of the year, i.e., during Spring–Summer.

In Fig. 8, the rainfall rates are plotted along with the emissivity trends. This parameter loses the seasonal periodicity because of the normalization to surface temperature. Furthermore, thanks to normalization, the variations due to the storm occurrences are better highlighted.

The differences in the dynamics of the radiometric quantities at the four frequencies are due to the different penetration capability through the vegetation canopy and to the different spatial resolutions of the four considered frequencies. The trends at Ka and X bands are similar to the ones at C band, but with a lower dynamic range. This is due to the higher canopy attenuation and to the reduced dynamics of soil permittivity of the higher frequencies. The enhanced dynamics of L band [Figs. 7(d) and 8(d)] with respect to other bands allows a better appreciation of the changes due to rainfall, flooding, and saturation of soil.

Vegetation effects are over imposed to the soil ones, especially at short wavelengths, but short-term variations in the microwave signature time series remain visible after rainfall or flooding and can be related to changes of soil properties also in presence of vegetation. Indeed, forests change very slowly their biomass, so that variations of the vegetation emission contribution are slower than variations due to rainfall or flooding. Interception or change

Fig. 7. AMSR-E and SMOS multifrequency time series of T_{BV}, T_{BH} plus ground truth data collected at rainfall stations, from Jan. 2010 to Oct. 2011. (a) AMSR-E Ka band. (b) AMSR-E X band. (c) AMSR-E C band. (d) SMOS L band.

in canopy moisture would produce an unpolarized emission, which would reduce the difference between the emission at vertical and horizontal polarizations [37]. However, in the case under study, an increase of this difference is observed after the
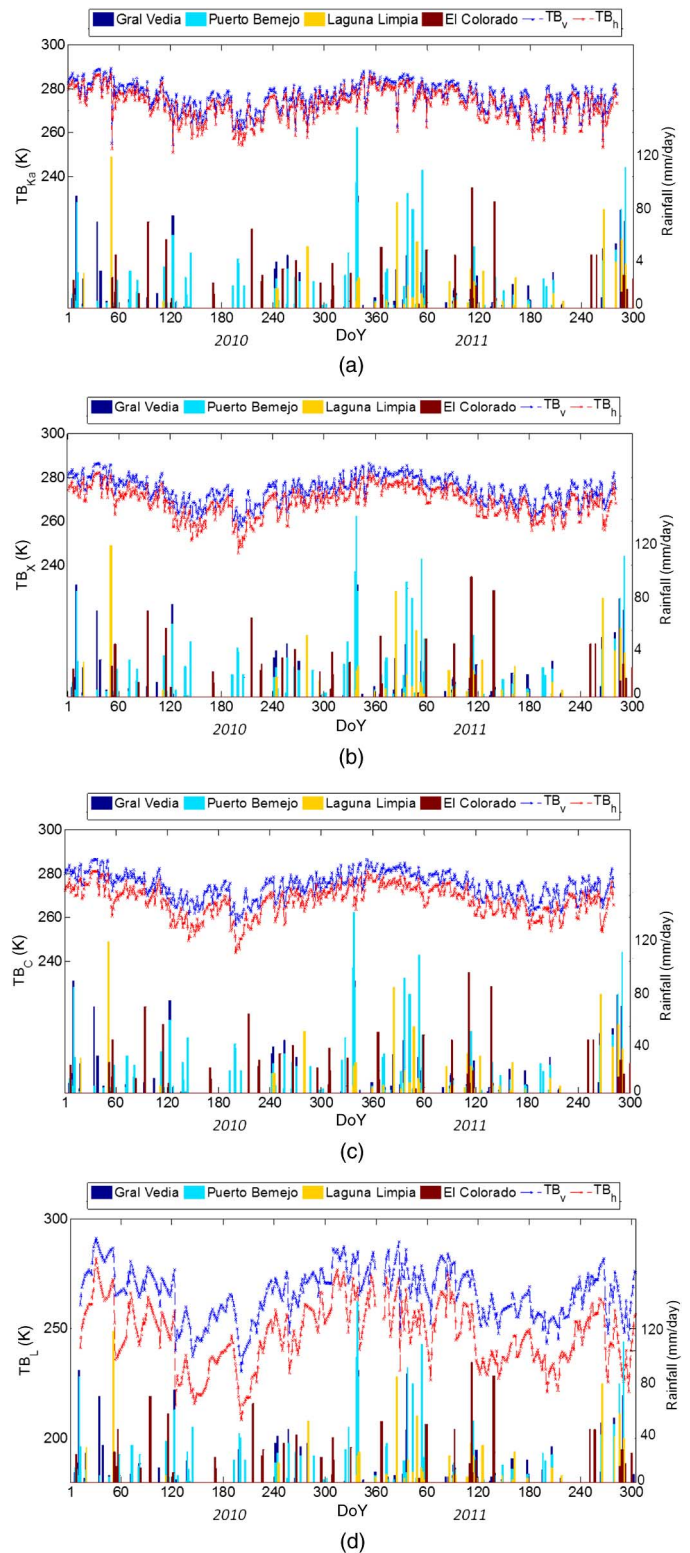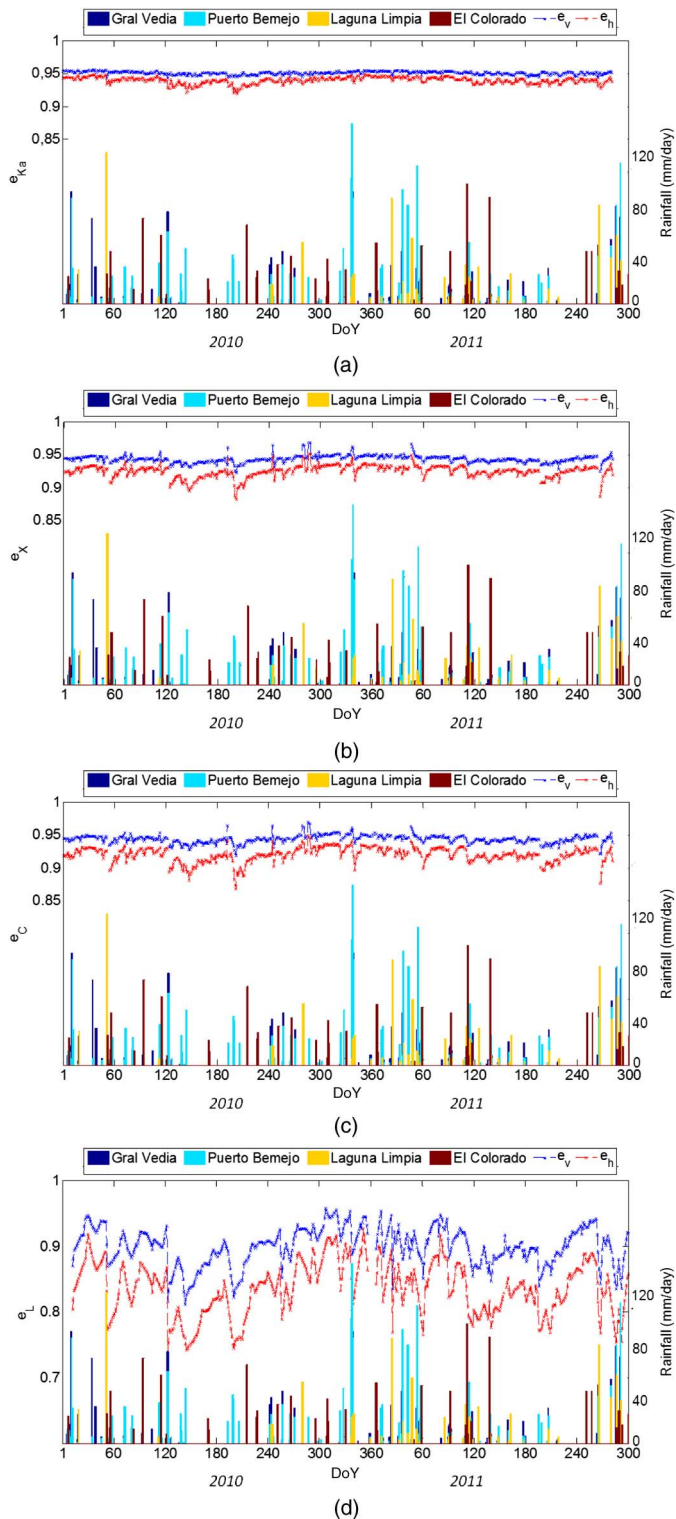
Fig. 8. AMSR-E and SMOS multifrequency time series of e_v, e_h plus ground truth data collected at rainfall stations, from Jan. 2010 to Oct. 2011. (a) AMSR-E Ka band. (b) AMSR-E X band. (c) AMSR-E C band. (d) SMOS L band.

rainfalls, so that emissivity variations can be attributed mainly to soil effects.

These considerations on the T_B and e series acquired by AQUA AMSR-E and SMOS-MIRAS instruments assured the reliability and congruence of the multifrequency and multitemporal datasets.

V. APPLICATION TO FLOOD FORECASTING

A. Algorithm

In Section IV, it has been shown that the emissivity signatures are driven by the sensitivity to dielectric properties of the observed surface, which may display a broad dynamic range of dielectric constant from dry to water surfaces. That is, Tb and e are sensitive to the soil saturation state which, being related to rain and runoff, can be a precursor of flooding events. The radiometric quantities are not directly correlated to water level in a watershed but to soil infiltration capacity and moisture antecedent conditions, which are among the main causes of flooding. Therefore, their information content could be exploited in flooding forecast. In order to test this hypothesis, we implemented the forecasting model of river water level which has been introduced in [26]. We selected this method since it is based on direct assimilation of remote sensing data, and it does not require hydraulic backgrounds. However, the conclusions drawn from this study can be of interest for the application of other forecasting methodologies. The model assumes a linear correlation between water level and input values, but it is able to perform a dynamic adjustment of the weight parameters as soon as new measurements are available as time flows. In this way, nonlinear trends of water level with time can be reproduced. We remark that in [26], the adaptive model was applied to a river basin in Australia, which differs from the Bermejo one for its structure, characterized by ephemeral channels in an arid region with scarce vegetation cover.

Detailed description of the adopted forecast model can be found in [26] and in the Appendix, where we also mention the adjustments which we introduced. Here, we mention that we selected the following inputs.

1) Rainfall measurements collected in the four meteorological stations surrounding El-Colorado site, since we assume that floods are related to local and upper basin precipitations.
2) Water level measurements performed at El Sauzalito station, about 300 km upstream El-Colorado site, in order to consider water flow propagation.
3) AMSR-E and SMOS emissivity at both polarizations. We disregarded brightness temperature measurements, since the seasonal surface temperature variations can mask the fluctuations due to change in soil conditions.

B. Results

First, we checked that the adopted algorithm could supply forecast values with reasonable accuracies. Then, we examined the performance of the AMSR-E and SMOS frequencies separately and in combination. The adaptive model has been applied to data of each satellite, considering three different forecast horizons (the L parameter) $L = 1$, $L = 3$, $L = 5$, and $L = 7$ days, whereas the number of days B included in the input measurements has been fixed to 7. The latter is related to the water travel time between El Sauzalito and El Colorado that is less than 1 week. Indeed, we have verified that the model results show a weak dependence on B.

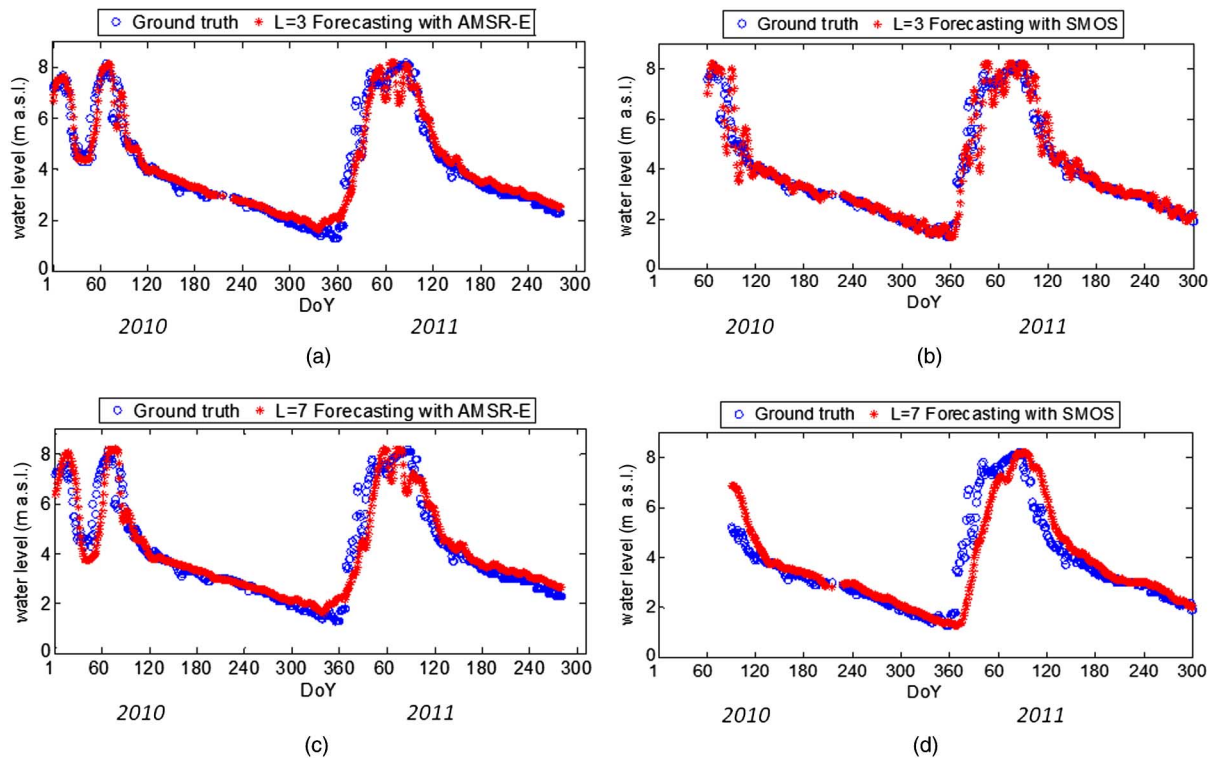Fig. 9 shows the water level forecast results for the hydrometric station of El Colorado obtained with emissivity

Fig. 9. Measured and predicted river water level values of El Colorado station. Forecasting using AMSR–E (left) and SMOS (right) emissivities. (a) and (b) Cases with forecast horizon equal to 3 days $L = 3$. (c) and (d) Cases with forecast horizon equal to 7 days $L = 7$. $B = 7$ in all cases.

measurements at Ka band of AMSR-E and at L-band of SMOS sensors. The predictions with lead time L equal to 5 days are not reported since they show an intermediate behavior between the 3 and 7 days results.

The results of Fig. 9 show that the forecasting algorithm is able to capture the real water level trend (blue circles in the figure), although with a certain delay which, nevertheless, decreases together with the forecast horizon. It can be observed that the forecast values of discharge peaks show a little dispersion around the ground truth values. These errors are always visible and become higher increasing more than 7 days the forecast horizon. Moderate differences are observed between results obtained with data collected by the two sensors.

In Fig. 10, the scatterplots worked out with measured and forecast values of water level at El Colorado station are shown. This representation highlights the adaptive model behavior with respect to the water level magnitude. The correlation coefficient (R) and the root mean squared error (RMSE) of the complete datasets are reported inside the graphs. The RMSE has been calculated comparing the predicted $Y(t)$ water level with the ground measurement $WL(t)$. We remark that t is the time when the measurement $WL(t)$ has been carried out. On its turn, the forecast value $Y(t)$ has been predicted L days earlier, i.e., at time $t - L$ (see also the Appendix), so that the forecast $Y(t)$ is independent from the observation $WL(t)$.

All plots show a good correlation between the estimated and the measured quantities, being R always larger than 0.9 and p-value lower than 5×10^{-5}. On its side, the RMSE shows the lowest values for the lowest lags. It can be also observed that the model presents higher variance for high water level values. For

this reason, we recomputed R and RMSE for two separate subsets of data: measured values of water level below and above 5 m. (We remind that flooding condition at El-Colorado station is met when 6 m water level is reached.) Table I reports the RMS errors obtained applying the forecast model to AMSR-E and SMOS frequencies and to the combination of Ka and L-band data. Other combinations were not reported since they yield intermediate results.

It can be noted that for $WL < 5$ m, R is always > 0.9 and the RMSE values are lower than 50 cm: during the dry season, i.e., when $WL < 5$ m, even $L = 5$ and $L = 7$ produce appreciable results. When $WL > 5$ m, the correlation R increases and the RMS error decreases when the forecast lead time decreases: during the rainy season, the adaptive algorithm requires a reduced lead time in order to get a more precise estimation of water level. In particular, when $L = 1$, the error in the prediction becomes lower than 10% of the measured water level. The lower accuracy of the highest lead times can be due to the loss of the linearity assumed by the adaptive model [(5) in the Appendix]. In particular, when water level changes very quickly, i.e., during the rainy period, the linear fit performed to find the weights W(t) of (5) might be inadequate to represent the water level variation, especially over long period of time, i.e., for large L values.

To evaluate the effectiveness of the satellite measurements in the river flow forecast, the adaptive model has been applied considering only the precipitation data and El Sauzalito water levels as input. The obtained results, shown in Fig. 11, highlight the role of the radiometric measurements. Indeed comparing the trend of the forecast values with the results of Fig. 9, the improvement introduced by the remote sensed AMSR-E and
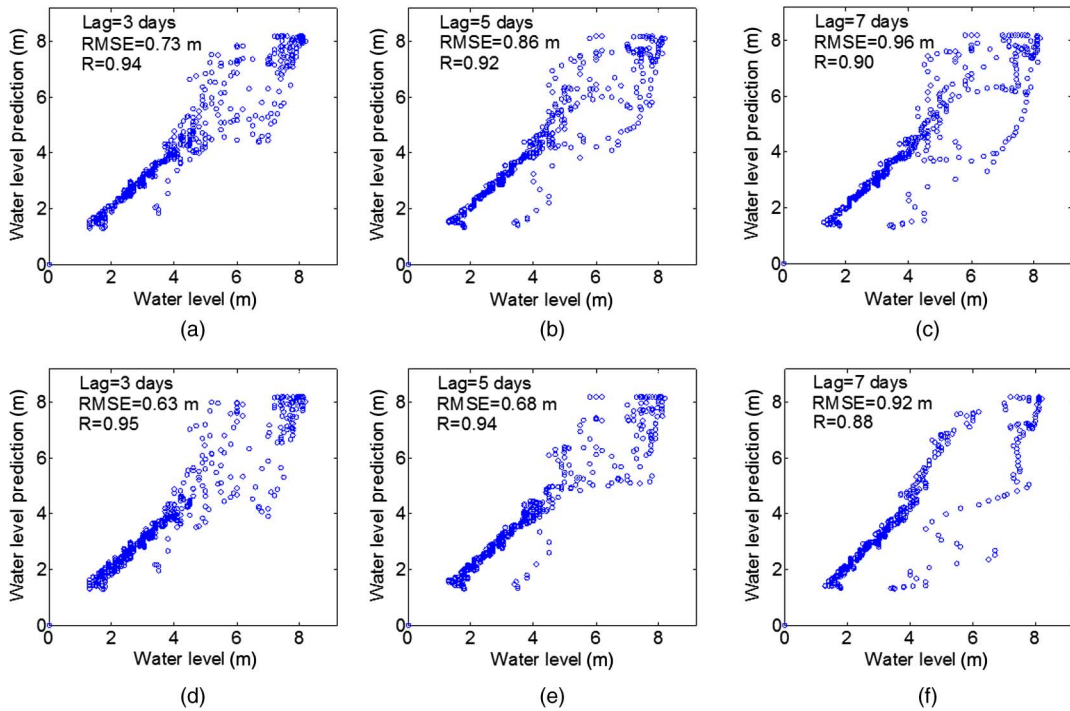
Fig. 10. Water level scatter plots obtained by $AMSR-E$ Ka band (top) and SMOS L-band (bottom) at (a) and (d) $L = 3$, (b) and (e) $L = 5$, and (c) and (f) $L = 7$. $B = 7$ in all cases.

TABLE I
RMSE AND R FOR EACH LEAD TIME FOR BOTH SENSORS

| 2010 2011	L=1, B=7				L=3, B=7				L=5, B=7				L=7, B=7			
	WL>5 m		WL>5 m		WL>5 m		WL>5 m		WL<5 m		WL>5 m		WL<5 m		WL>5 m	
	RMSE (m)	R	RMSE (m)	R	RMSE (m)	R	RMSE (m)	R	RMSE (m)	R	RMSE (m)	R	RMSE (m)	R	RMSE (m)	R
C	0.21	0.97	0.50	0.87	0.28	0.96	0.73	0.71	0.34	0.93	1.00	0.53	0.41	0.93	1.51	0.33
X	0.21	0.97	0.50	0.87	0.28	0.96	0.73	0.72	0.34	0.95	1.00	0.55	0.40	0.93	1.50	0.33
Ka	0.21	0.98	0.48	0.88	0.28	0.96	0.69	0.80	0.34	0.94	0.97	0.64	0.40	0.94	1.46	0.37
L	0.20	0.98	0.47	0.88	0.37	0.95	0.70	0.85	0.39	0.94	0.87	0.56	0.42	0.92	0.91	0.61
Ka+L	0.19	0.98	0.45	0.93	0.26	0.96	0.63	0.87	0.32	0.94	0.92	0.69	0.39	0.93	1.36	0.47
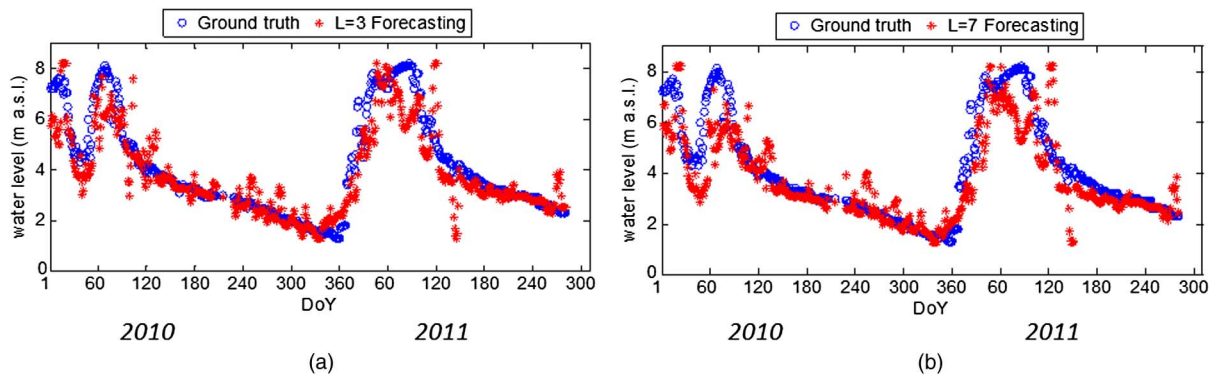
Fig. 11. Measured and predicted river water level values of El Colorado station without inclusion of satellite radiometric measurements in the model. (a) Forecast horizon $L = 3$. (b) Forecast horizon $L = 7$.

TABLE II
RMSE AND R FOR EACH LEAD TIME AND WITHOUT THE SATELLITE RADIOMETRIC DATA

2010 2011	L=3, B=7				L=5, B=7				L=7, B=7			
	WL<5 m		WL>5 m		WL<5 m		WL>5 m		WL<5 m		WL>5 m	
	RMSE	R	RMSE	R	RMSE	R	RMSE	R	RMSE	R	RMSE	R
Ground data	0.80 m	0.65	2.91 m	0.23	0.79 m	0.63	3.26 m	0.22	0.81 m	0.66	3.69 m	0.41

SMOS data is apparent. In particular, we remark that the absence of satellite radiometric measurements affect forecasting not only during the flooded days but also during the dry season. This is displayed by the higher RMSE's of the modeled data, which are reported in Table II.

Finally, we come back to Table I, and observe that the best forecasting results are obtained when using Ka or L band, or a combination of the two. These frequencies own different characteristics which turn out to be crucial for flood monitoring: thanks to its spatial resolution, the highest frequency data contain information about water surface extent that, on its turn, is correlated with river discharge [23]–[25]; the lowest frequency shows a remarkable sensitivity to soil conditions, forerunners of flooding. Indeed, L band provides the best sensitivity to variations in the soil, coupled with minimal disturbance from vegetation cover.

VI. CONCLUSION

In this work, the direct comparison between data acquired over the same area from satellite platforms, in a large microwave frequency range, has been performed. The same dataset has been subsequently employed in the application of an adaptive approach to the forecast of river water level. We selected the Argentinean lower Bermejo basin, where regular floods occur during the rainy season, together with AMSR-E data and the recently available SMOS radiometric measurements. The attractiveness in the use of the lower frequencies of AMSR-E and SMOS sensors is mainly due to the sensitivity of the microwave bands to the soil saturation, as well as to the high time resolution of the data. The analysis has been carried out along a 2-year time frame (2010–2011) during which the two sensors were simultaneously active and two flood events occurred.

The preliminary analysis confirmed the expected theoretical behavior of the brightness temperature and emissivity at L, C, X, and Ka bands with respect to rain and flooding events. The obtained results suggested the idea to test the performance of multifrequency radiometric data for river water level forecasting, using e variations together with rainfall rates. It is well known that changes in emissivity at Ka band are correlated with changes in water surface extent within the pixel, whereas lower frequencies are sensitive to soil moisture changes. So, even though the measured radiometric quantities are not directly correlated with streamflow, they can play an important role in the prediction task, being sensitive to surface conditions prone to saturation and to

development of floodings. Thus, an adaptive model has been chosen which takes as input radiometric data.

Comparable forecast results were obtained at all frequencies. However, the best performances are achieved at Ka and L bands, showing that the higher resolution of the highest frequencies is counterbalanced by the highest sensitivity to soil conditions at the lowest frequencies. The results of this paper, therefore, encourage the employment of L band microwave radiometry in the monitoring of flood evolution. In particular, the performance of advanced and skilled forecasting methods can benefit from SMOS and SMAP data.

In a real application context, these radiometric data could be integrated in operational flood forecasting systems. Furthermore, the water gauge and meteorological measurements, eventually needed by predictive algorithms, could be substituted by altimetric data and rain data measured from spaceborne platforms as well. Indeed, the high resolution altimetry Surface Water Ocean Topography mission and Global Precipitation Measurement mission will open new scenarios for a system completely based on the assimilation of remote sensing data [38].

APPENDIX

In order to find the relation that can describe the correlation between satellite and ground truth hydrometric variations, Bindlish *et al.* [26] developed an adaptive model which performs a linear fit between input and output, and dynamically adjusts the weights, depending on the evolving conditions. We implemented this model and tested it for the area around El Colorado in the lower Bermejo basin. This site counts the major number of seasonal floods, and water peaks always occur from January to March (rainy season), so that it has been possible to follow the evolution of two floods. The algorithm has been applied to measurements from AMSR-E and SMOS, in concomitant operation between 2010 and 2011, with slight differences in the vector of inputs, as shown in (4a) and (4b).

The model inputs are:
1) measurements of AMSR-E e_{vf} and e_{hf} or the SMOS e_{vL} and e_{hL}, extracted from the rectangular box (26°–26.5°S latitude and 59°–59.5°W longitude) that includes El Colorado station;
2) ground rainfall measurements in the four rainfall stations closer to El Colorado hydrometric station P_k with k = 1, 4;
3) water level WL_{ElS} measured in the upstream hydrometric station of El Sauzalito.

The model output consists of the estimation, hereafter called Y, of the water level ground observations at El Colorado station (WL). The latter is the ground truth which is ingested by the algorithm as soon as it comes available.

The water level $Y(t + L)$ is forecast at a time t, i.e., a given Day of the Year, for the following day $t + L$. The lead time (or forecast horizon) L, equal to 1, 3, 5, or 7 days, represents the time that a prediction is made for, and is related to the alert time in a river basin. The model has been developed under the hypothesis of linear dependence of the water level from the model inputs acquired B days in the past, as summarized in (3)

$$Y(t + L) = \boldsymbol{W}(t)^T \boldsymbol{X}(t). \tag{3}$$

In (3), $\boldsymbol{W}(t)$ is the weight vector and $\boldsymbol{X}(t)$ is the input vector. The latter is actually representative of a stream of data; i.e., the components of this vector represent the previously listed parameters, acquired during B days before the day t. The expanded formulations of $\boldsymbol{X}(t)$ for the AMSR-E and the SMOS are shown in (4a) and (4b), respectively

$$\boldsymbol{X}(t) = (P_1(i), P_2(i), P_3(i),$$
$$P_4(i), e_{vf}(i), e_{hf}(i), WL_{ElS}(i))_{i=t-B+1,t} \tag{4a}$$
$$\boldsymbol{X}(t) = (P_1(i), P_2(i), P_3(i),$$
$$P_4(i), T_{BvL}(i), T_{BhL}(i), WL_{ElS}(i))_{i=t-B+1,t}. \tag{4b}$$

At each new day, $\boldsymbol{X}$ is updated with the new incoming data. Therefore, at a given t, $\boldsymbol{X}$ contains the information acquired in the previous B days, i.e., from day $t - B + 1$ to t. Such a choice depends on the observation that, when flooding occurs, the saturation of soil depends on the soil condition present some days before the flooding itself. Furthermore, B is connected to the hydrological behavior of the selected area and can be varied according to intrinsic features of the basin, like geophysical and topographical ones.

L represents the number of days after the observations when the river level is to be forecast. B represents the number of days before a certain time t that enter the model as input. As a consequence, B indicates the number of components for each variable considered in the vector of inputs. In the original model by Bindlish et $al.$ [26], B = L. We relaxed this constraint since we could take advantage of B measurements made in the past in order to predict water level at L days in the future.

A linear interpolation has been applied when data necessary to build X were not available (AMSR-E and SMOS e_{pf}, or El Sauzalito water levels, WL), in order to guarantee a uniform temporal resolution of 1 day.

Through an adaptive algorithm, the model performs the dynamic daily changing of the weights when new observations come. Each prediction is performed with weights whose modification depends on the radiometric responses, as well as on precipitations and on the measured water level in the upstream station, of B days in the past. This allows building a flexible model that is able to perform a linear fit at each time t. From one time t to the next, the weight vector W is dynamically adapted using the least mean square (LMS) algorithm [39], [40]: in this way, nonlinear trends are represented by spline functions. The
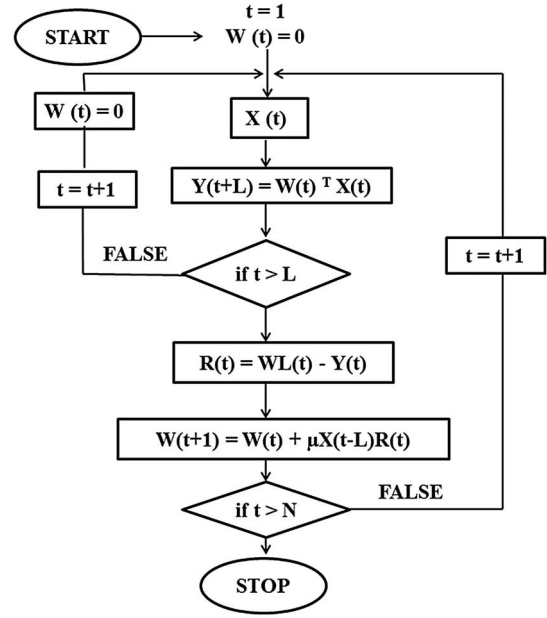

Fig. 12. Algorithm flowchart.

vector of weights has not been initialized, i.e., $W(t) = 0$, for $t = 1, L + 1$.

L days after the forecasting, the water level $WL(t)$ is measured at El Colorado station, and it is used to compute the residual error (R) between the ground truth and the model output

$$R(t) = WL(t) - Y(t). \tag{5}$$

In (5), $Y(t)$ is the estimation of water level at time t, i.e., the forecast value computed by means of the inputs $\boldsymbol{X}(t - L)$. $WL(t)$ is the ground truth water level measured at El Colorado station at time t.

The residual error is used at each step to adjust the vector of weights applying the LMS formulation

$$\boldsymbol{W}(t + 1) = \boldsymbol{W}(t) + \mu \boldsymbol{X}(t - L)R(t) \tag{6}$$

where the values for the weights are computed considering their previous values and an added term given by the residual error $R(t)$ multiplied by the input $X(t - L)$ and by the step size parameter μ, a positive constant which is required for the convergence of the algorithm [39]. In our study, we chose $0.0003 < \mu < 0.0012$, when using the AMSR-E data, and $0.095 < \mu < 0.024$ for SMOS. This selection was made applying the forecasting algorithm on a training dataset; i.e., we chose the μ value yielding the lowest RMSE on data collected in the whole 2009 by AMSR-E and on the first 60 days of 2010 by SMOS.

In order to better understand the methodology used here, a flowchart has been developed (Fig. 12).

As explained in the figure, at the first steps, the weights $W(t)$ are initialized to zero. Therefore, the first $L + 1$ inputs $\boldsymbol{X}(t)$, i.e., the inputs for the first L predictions, produce forecasts $Y(L + 1)$ to $Y(2L + 1)$ equal to zero. This means that the first residual errors $R(L + 1)$ to $R(2L + 1)$, computed as soon as the water level is measured, will be equal to the ground truth $WL(t)$, or rather the hydrometric value acquired at the days $L + 1$ to

$2L + 1$. As a consequence, the forecasting $Y(t + L)$ performed at $t = L + 2$ to $2(L + 1)$ cannot be considered significant. This first phase of the algorithm can be called "initialization phase" and it lasts $2(L + 1)$ days. In our study, we included the initialization phase inside the training phase, previously described. In the subsequent steps, the LMS algorithm adjusts the weights in order to minimize the residual errors at each step, according to (6). The algorithm is stopped when the last water level measurement is available (e.g., at time N), which allows the prediction at time $N + L$.

References

[1] H. Madsen and C. Skotner, "Adaptive state updating in real-time river flow forecasting: A combined filtering and error forecasting procedure," *J. Hydrol.*, vol. 308, no. 1, pp. 302–312, Jul. 2005.

[2] A. de Roo *et al.*, "Development of a European flood forecasting system," *Int. J. River Basin Manag.*, vol. 1, no. 1, pp. 49–59, Aug. 2003.

[3] J. Bartholmes and E. Todini, "Coupling meteorological and hydrological models for flood forecasting," *Hydrol. Earth Syst. Sci.*, vol. 9, no. 4, pp. 333–346, Nov. 2005.

[4] R. Krzysztofowicz, "Bayesian theory of probabilistic forecasting via deterministic hydrologic model," *Water Resour. Res.*, vol. 35, no. 9, pp. 2739–2750, Jul. 1999.

[5] A. Porporato and L. Ridolfi, "Multivariate nonlinear prediction of river flows," *J. Hydrol.*, vol. 248, no. 1, pp. 109–122, Jul. 2001.

[6] M. Bruen and J. Yang, "Functional networks in real-time flood forecasting a novel application," *Adv. Water Resour.*, vol. 28, no. 9, pp. 899–909, Sep. 2005.

[7] E. Todini, "Role and treatment of uncertainty in real time flood forecasting," *Hydrol. Processes*, vol. 18, no. 14, pp. 2743–2746, Oct. 2004.

[8] J. M. Jacobs, D. A. Myers, and B. M. Whitfield, "Improved rainfall/runoff estimates using remotely sensed soil moisture," *J. Amer. Water Resour. Assoc.*, vol. 39, no. 2, pp. 313–324, Jun. 2003.

[9] M. P. Clark *et al.*, "Hydrological data assimilation with the ensemble Kalman filter: Use of streamflow observations to update states in a distributed hydrological model," *Adv. Water Resour.*, vol. 31, pp. 1309–1324, 2008.

[10] G. Schumann, P. D. Bates, M. S. Horritt, P. Matgen, and F. Pappenberger, "Progress in integration of remote sensing derived flood extent and stage data and hydraulic models," *Rev. Geophys.*, vol. 47, no. 4, p. RG4001, Nov. 2009.

[11] V. Pauwels, R. Hoeben, N. E. C. Verhoest, and F. P. De Troch, "The importance of the spatial patterns of remotely sensed soil moisture in the improvement of discharge predictions for small-scale basins through data assimilation," *J. Hydrol.*, vol. 251, no. 1, pp. 88–102, Sep. 2001.

[12] P. D. Bates, M. S. Horritt, L. C. Smith, and D. C. Mason, "Integrating remote sensing observations of flood hydrology and hydraulic modeling," *Hydrol. Processes*, vol. 11, no. 14, pp. 1777–1795, Nov. 1997.

[13] J. B. Henry, P. Chastanet, K. Fellah, and Y. L. Desnos, "ENVISAT multipolarised ASAR data for flood mapping," *Int. J. Remote Sens.*, vol. 27, pp. 1921–1929, 2006.

[14] L. L. Hess, J. M. Melack, E. M. L. M. Novo, C. C. F. Barbosa, and M. Gastil, "Dual-season mapping of wetland inundation and vegetation for the central Amazon basin," *Remote Sens. Environ.*, vol. 87, pp. 404–428, 2003.

[15] M. S. Horritt, D. C. Mason, and A. J. Luckman, "Flood boundary delineation from synthetic aperture radar imagery using a statistical active contour model," *Int. J. Remote Sens.*, vol. 22, pp. 2489–2507, 2001.

[16] G. Schumann, G. Di Baldassarre, and P. D. Bates, "The utility of spaceborne radar to render flood inundation maps based on multialgorithm ensembles," *IEEE Trans. Geosci. Remote Sens.*, vol. 50, no. 7, pp. 2801–2807, Aug. 2009.

[17] L. Pulvirenti, M. Chini, N. Pierdicca, L. Guerriero, and P. Ferrazzoli, "Flood monitoring using multi-temporal COSMO-SkyMed data: Image segmentation and signature interpretation," *Remote Sens. Environ.*, vol. 115, no. 4, pp. 990–1002, Apr. 2011.

[18] L. Pulvirenti, N. Pierdicca, M. Chini, and L. Guerriero, "Monitoring flood evolution in vegetated areas using COSMO-SkyMed data: The Tuscany 2009 case study," *IEEE J. Sel. Topics Appl. Observ. Remote Sens.*, vol. 6, no. 4, pp. 1807–1816, Aug. 2013.

[19] D. M. Bjerklie, D. Moller, L. C. Smith, and S. L. Dingman, "Estimating discharge in rivers using remotely sensed hydraulic information," *J. Hydrol.*, vol. 309, pp. 191–209, 2005.

[20] D. E. Alsdorf, E. Rodriguez, and D. P. Lettenmaier, "Measuring surface water from space," *Rev. Geophys.*, vol. 45, no. 2, pp. 1–24, Jun. 2007.

[21] G. R. Brakenridge, S. V. Nghiem, E. Anderson, and R. Mic, "Orbital microwave measurements of river discharge and ice status," *Water Resour. Res.*, vol. 43, 16 p., 2007, W04405.

[22] Z. Kugler and T. DeGroeve, "The global flood detection system," JRC Sci. Tech. Rep. JRC 44149, 2007.

[23] G. R. Brakenridge *et al.*, "Calibration of satellite measurements of river discharge using a global hydrology model," *J. Hydrol.*, vol. 475, pp. 123–136, 2012.

[24] S. I. Khan *et al.*, "Microwave satellite data for hydrological modeling in ungauged basins," *IEEE Geosci. Remote Sens. Lett.*, vol. 9, no. 4, pp. 663–667, Jul. 2012.

[25] F. A. Hirpa *et al.*, "Upstream satellite remote sensing for river discharge forecasting: application to major rivers in South Asia," *Remote Sens. Environ.*, vol. 113, pp. 140–151, 2013.

[26] R. Bindlish, W. T. Crow, and T. J. Jackson, "Role of passive microwave remote sensing in improving flood forecasts," *IEEE Geosci. Remote Sens. Lett.*, vol. 6, no. 1, pp. 112–116, Jan. 2009.

[27] J. Brea, M. Busquets, and P. Spalletti, "Análisis de la dinámica fluviomorfológica del río Bermejo Inferior," Informe LHA, 178-02, 1999.

[28] J. Morello and J. Adámoli, "Las grandes unidades de vegetación y ambiente del Chaco argentino. Segunda Parte: Vegetación y ambiente de la Provincia del Chaco," *INTA Ser. Fitogeográfica*, vol. 13, p. 130, 1974.

[29] T. Kawanishi *et al.*, "The advanced microwave scanning radiometer for the earth observing system (AMSR-E), NASDA's contribution to the EOS for global energy and water cycle studies," *IEEE Trans. Geosci. Remote Sens.*, vol. 41, no. 2, pp. 184–194, Feb. 2003.

[30] K. Nakagawa, "GCOM-W and GCOM-C project status," in *Proc. IEEE Int. Geosci. Remote Sens. Symp. (IGARSS'10)*, Jul. 2010, pp. 1355–1358.

[31] R. A. M. De Jeu *et al.*, "Global soil moisture patterns observed by space borne microwave radiometers and scatterometers," *Surveys Geophys.*, vol. 29, no. 4–5, pp. 399–420, Oct. 2008.

[32] M. Fily, A. Royer, K. Goita, and C. Prigent, "A simple retrieval method for land surface temperature and fraction of water surface determination from satellite microwave brightness temperatures in sub-arctic areas," *Remote Sens. Environ.*, vol. 85, no. 3, pp. 328–338, May 2003.

[33] R. M. Parinussa, T. R. H. Holmes, and R. A. M. de Jeu, "Soil moisture retrievals from the WindSat spaceborne polarimetric microwave radiometer," *IEEE Trans. Geosci. Remote Sens.*, vol. 50, no. 7, pp. 2683–2694, Jul. 2012.

[34] Y. H. Kerr *et al.*, "The SMOS soil moisture retrieval algorithm," *IEEE Trans. Geosci. Remote Sens.*, vol. 50, no. 5, pp. 1384–1403, May 2012.

[35] Y. H. Kerr *et al.*, "Soil moisture retrieval from space: The Soil Moisture and Ocean Salinity (SMOS) mission," *IEEE Trans. Geosci. Remote Sens.*, vol. 39, no. 8, pp. 1729–1735, Aug. 2001.

[36] C. Vittucci *et al.*, "Study of multifrequency sensitivity to soil moisture variations in the lower Bermejo basin," *Eur. J. Remote Sens.*, vol. 46, pp. 775–788, 2013.

[37] K. Saleh *et al.*, "Estimates of surface soil moisture under grass covers using L-band radiometry," *Remote Sens. Environ.*, vol. 109, no. 1, pp. 42–53, Jul. 2007.

[38] M. Durand *et al.*, "The surface water and ocean topography mission: Observing terrestrial surface water and oceanic submesoscale eddies," *Proc. IEEE*, vol. 98, no. 5, pp. 766–779, May 2010.

[39] S. Haykin, *Adaptive Filter Theory*. Englewood Cliffs, NJ, USA: Prentice Hall, 1991.

[40] B. Farhang-Boroujeny, *Adaptive Filters: Theory and Applications*. Hoboken, NJ, USA: Wiley, 1998.

Cristina Vittucci received the M.Sc. degree in environmental engineering from the University "La Sapienza" of Rome, Rome, Italy, and the Master degree in remote sensing and GIS for environmental planning from the University of Roma Tre, Rome, Italy, in 2007 and 2009, respectively.

Since 2010, she has joined the Microwave Remote Sensing Group, Tor Vergata University, Rome, Italy. During her Ph.D., she took part in the Third Soil Moisture Active Passive Experiment (SMAPEx-3), NSW, Australia, in 2011. Her research interests include the use of soil moisture observations, obtained by active and passive microwave sensors, for improving hydrological applications.

Leila Guerriero (M'11) received the Laurea degree in physics from Sapienza University, Rome, Italy, and the Ph.D. degree in electromagnetism from the University of Rome Tor Vergata, Rome, Italy, in 1986 and 1991, respectively.

Since 1994, she has been a permanent Researcher at Tor Vergata University, where she is now an Associate Professor holding a course on Earth Satellite Monitoring. Her research interests include modeling microwave scattering and emissivity from agricultural and forested areas. In 1988, she was involved in cooperation between JPL and Italian National Research Council for investigations on geophysical applications of Imaging Spectrometry in InfraRed and Visible Remote Sensing. In 1995, she participated in the ESA project on Radiometric Polarimetry of Ocean Surfaces. In 1999–2001, she participated at the EEC concerted action ERA-ORA whose objective was to improve radar data analysis and utilization. More recently, she has been part of the teams of the ESA projects "Soil Moisture and Ocean Salinity Satellite," "Development of SAR Inversion Algorithms for Land Applications," "Use of Bistatic Microwave Measurements for Earth Observation," "LEIMON: Land Monitoring with Navigation Signals," and "GRASS: GNSS-Reflectometry Analysis for Biomass Monitoring."

Dr. Guerriero is a member of the Scientific Committee of MicroRad.

Paolo Ferrazzoli (M'94–SM'06) graduated from the University "La Sapienza" of Rome, Rome, Italy, in 1972.

In 1974, he joined Telespazio s.p.a., where he was mainly active in the fields of antennas, slant-path propagation, and advanced satellite telecommunication systems. In 1984, he joined Tor Vergata University of Rome, Rome, Italy, where he is presently working, teaching microwaves, propagation, and electromagnetic fields. He has been involved in international experimental remote sensing campaigns such as AGRISAR, AGRISCATT, MAESTRO-1, MAC-Europe, and SIR-C/X-SAR. He has participated in the coordinating team of ERA-ORA Project, funded by EEC, establishing an assemblage among several European researchers working in radar applications. His research interests include microwave remote sensing of vegetated terrains, with particular emphasis on electromagnetic modeling.

Mr. Ferrazzoli has been a member of the Science Advisory Group and is a member of Quality Working Group in the framework of ESA SMOS project. He was Chair of MICRORAD 2012 International Meeting, and a member of Technical Program Committee of IGARSS 2012, IGARSS 2013, and IGARSS 2014 Conferences.

Rachid Rahmoune received the B.Sc. degree in physics from Hassan II University, Casablanca, Morocco, the M.Sc. degree in remote sensing, from Istituto Superiore Universitario di Formazione Interdisciplinare (ISUFI), University of Lecce, Lecce, Italy, and the Ph.D. degree in geoinformation from Tor Vergata University, Rome, Italy.

From 2003 to 2007, he was with the Remote Sensing Group, Department of Physics, Polytechnic University of Bari, Bari, Italy. Since 2008, he has been with the Microwave Remote Sensing Group, Tor Vergata University, Rome, Italy. His research interests include electromagnetic modeling of vegetated areas, particularly to forests and retrieval of bio-geophysical parameters from MIRAS radiometer on-board SMOS Satellite.

Verónica Barraza received the degree in biology in 2009 from the Universidad Nacional de la Patagonia San Juan Bosco (UNPSJB), Chubut, Argentina, and has been pursuing the Ph.D. degree at the University of Buenos Aires (UBA), Buenos Aires, Argentina since 2011.

She joined the Institute of Astronomy and Space Physics (IAFE), CABA, Argentina, 4 years ago. Her research interests include remote sensing to study and analyze broad-scale vegetation health and functioning.

Francisco Grings is a Researcher with the Institute of Astronomy and Space Physics (IAFE), Buenos Aires, Argentina. His current interests include retrieval of soil moisture using active/passive microwave data and satellite-based monitoring of water cycle in general (e.g., flood condition and plant water stress).